

Water Detection in SWOT HR Images Based on Multiple Markov Random Fields

Sylvain Lobry *Member, IEEE*, Loïc Denis *Member, IEEE*, Brent Williams *Member, IEEE*, Roger Fjørtoft *Member, IEEE*, Florence Tupin *Senior Member, IEEE*,

Abstract—One of the main objectives of the Surface Water and Ocean Topography (SWOT) mission, scheduled for launch in 2021, is to measure inland water levels using synthetic aperture radar (SAR) interferometry. A key step towards this objective is to precisely detect water areas. In this article, we present a method to detect water in SWOT images. Water is detected based on the relative brightness of the water and non-water surfaces. Water brightness varies throughout the swath because of system parameters (i.e., the antenna pattern), as well as the phenomenology such as wind speed and surface roughness. To handle the effects of brightness variability, we propose to model the problem with one Markov Random Field (MRF) on the binary classification map, and two other MRFs to regularize the estimation of the class parameters (i.e., the land and water background power images). Our experiments show that the proposed method is more robust to the expected variations in SWOT images than traditional approaches.

Index Terms—SAR, InSAR, water detection, binary classification, Markov Random Fields

I. INTRODUCTION

THE Surface Water and Ocean Topography (SWOT) [1] mission is an innovative altimetry mission projected for launch in 2021. It is prepared jointly by the National Aeronautics and Space Administration (NASA) and the French Space Agency "Centre National d'Etudes Spatiales" (CNES), with contributions from the Canadian Space Agency (CSA) and the United Kingdom Space Agency (UKSA). The main satellite payload is a Ka-band Radar Interferometer (KaRIn) [2]. This Interferometric Synthetic Aperture Radar (InSAR) has two modes: the high-rate (HR) mode dedicated to continental hydrology, and the low-rate (LR) mode dedicated to oceanography. The principal objectives of the mission is to measure Sea Surface Height (SSH) and inland water levels and extents at unprecedented spatial resolutions. One of the main science requirements for continental water surfaces is to detect lakes and reservoirs larger than $250 \times 250 \text{ m}^2$ (goal:

S. Lobry is with the Laboratory of GeoInformation Science and Remote Sensing, Wageningen University, 6708 PB Wageningen, The Netherlands. Most of the work presented in this article was made during the PhD of S. Lobry at the LTCI, Télécom Paris, Institut Polytechnique de Paris, France, financed by CNES and the Futur&Ruptures program of the Fondation Mines-Télécom. L. Denis is with Univ Lyon, UJM-Saint-Etienne, CNRS, Institut d'Optique Graduate School, Laboratoire Hubert Curien UMR 5516, F-42023, SAINT-ETIENNE, France. B. Williams is with the Jet Propulsion Laboratory, California Institute of Technology, Pasadena, CA 91109, USA. R. Fjørtoft is with the Centre National d'Etudes Spatiales (CNES), 31401 Toulouse, France. F. Tupin is with the LTCI, Télécom Paris, Institut Polytechnique de Paris, France.

Manuscript received June 18, 2019; revised September 19, 2019; accepted October 10, 2019.

$100 \times 100 \text{ m}^2$) and rivers wider than 100 m (goal: 50 m), with a relative surface area error below 15% and a height error below 10 cm after averaging over 1 km^2 [3]. The focus of this study is to detect inland water in the HR mode.

Water detection is one of the key steps in the operational processing of SWOT HR data, and can be considered as a binary classification task. SAR images, due to their coherent nature, are corrupted by speckle which can be modeled as a strong multiplicative noise. For this reason, methods which classify a pixel independently from its neighbors generally yield poor results. A strategy which has been used to cope with this problem is to regularize the image before detecting water areas. In [4], the Lee filter [5] is applied first, followed by a classical anisotropic filter [6] to enhance edges (despeckled data is assumed to follow a Gaussian distribution). In [7], the same anisotropic filter [6] is applied before hysteresis thresholding to detect flooding in SAR data. A filter for non-stationary speckle reduction [8] is used prior to water detection in [9]. A non-local speckle filtering method [10] could also be used.

Another family of approaches is based on prior segmentation of the image. Once a good segmentation has been found (i.e., with sufficiently large and homogeneous regions to reliably estimate class parameters) the actual classification can be made based on these statistics. This problem can be solved through edge detection based on a ratio operator [11], [12] followed by a watershed algorithm [13] to extract closed and skeleton edges. Another option is to use an active contour algorithm that is able to handle multiple regions. In [14] the classical formulation of [15] is adapted to SAR images for water segmentation using log-normal distributions to model the statistics.

While these approaches can give good results in many cases, they generally either 1) assume constant class parameters, which is generally not a good assumption for SWOT surface water images, or 2) do not employ prior information about the brightness, nor abundance, of certain surface classes, including water. In this article, we present a method to detect water in SWOT images that takes into account the spatial variations in the class parameters, while loosely incorporating knowledge about the prior brightness of water relative to non-water surfaces, as well as hypotheses about the spatial regularity of water bodies. This method also can enable prior knowledge of the probability of water occurrence in a given region.

The proposed method is described in section III, and assessed on simulated SWOT images in section IV, where it is identified as a promising candidate for SWOT baseline

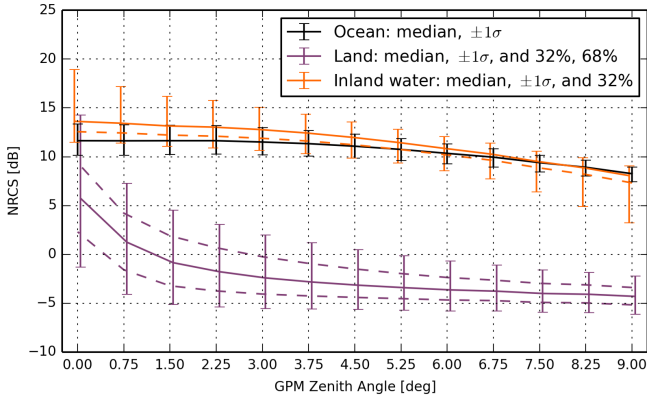


Fig. 1. Ka-band σ_0 as a function of incidence measured by the Global Precipitation Measurement (GPM) mission over ocean, land and inland water surfaces [17].

processing. Note that the purpose and scope of this paper is not to conduct a full validation of the method, but to present the theoretical framework and some preliminary analysis, whereon a more complete validation can be carried out by the SWOT Algorithm Development Team (ADT).

II. SWOT WATER DETECTION PHENOMENOLOGY

The fact that KaRIn/SWOT acquires SAR images very close to nadir and at Ka-band means that there are some significant differences with respect to existing Earth observing spaceborne SAR systems that operate at higher incidence angles and longer wavelengths [16]. In particular, in the incidence range of KaRIn/SWOT (0.6° - 3.9°), water is expected to have a generally brighter backscatter than land. The use of Ka-band provides higher sensitivity to small-scale water roughness than longer wavelengths (e.g. X, C or L-band).

Figure 1 summarizes low-incidence Ka-band σ_0 measured by the Global Precipitation Measurement (GPM) mission over ocean, land and inland water surfaces [17].

We see in this figure that the σ_0 of inland water is generally above 10 dB, whereas that of land is typically on the order of 10 dB lower in the incidence range of KaRIn.

However, there are several exceptions to this nominal situation:

- At very low wind speed (<1-2 m/s) and in the absence of turbulence, the water will basically act as a plane mirror so that little or no signal is backscattered towards the radar [16], causing patches of dark water in the acquired SAR images.
- Some land surfaces can be expected to be bright (e.g., roads, urban areas, hills/mountains causing land/land lay-over).
- Rain and vegetation attenuate the surface signal.

Another property of KaRIn to keep in mind is that the noise-equivalent σ_0 is very high compared to conventional spaceborne SAR systems, because of power budget constraints (continuous acquisition on both sides of the satellite track). Figure 2 shows the noise-equivalent σ_0 of a single-look complex (SLC) image produced by KaRIn in HR mode as

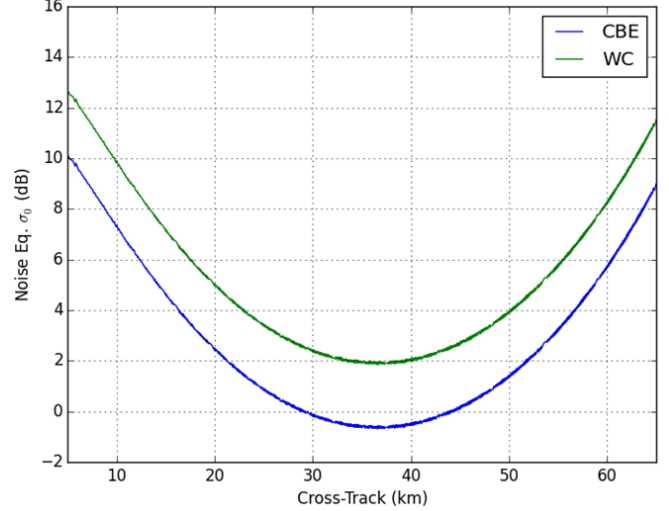


Fig. 2. Noise-equivalent σ_0 for single-look complex SWOT HR image as a function of incidence (CBE: current best estimate, WC: worst case)

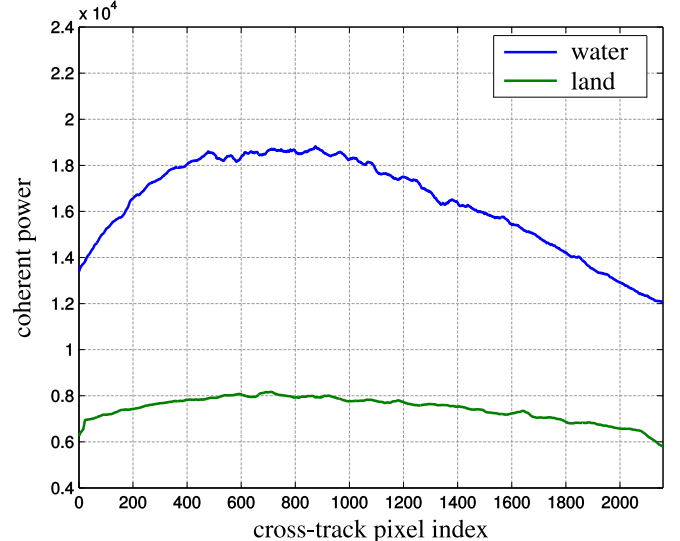


Fig. 3. Example of the average coherent power across the swath for water (blue) and land (green).

a function of the position in the swath, for both the current best estimate (CBE) and the $1-\sigma$ worst case (WC) scenario. We see that it is around 0 dB in the middle of the swath, rising to 6-7 dB in the beginning (10 km) and towards the end (60 km) of the nominal swath, in the CBE case (WC is 2-3 dB above). The shape of the graphs reflects instrument properties, mainly the antenna pattern. It should be noted that the signal-to-noise ratio (SNR) can be improved by up to 3 dB by combining the two interferometric channels coherently, i.e. summing the two coregistered SLCs after tentatively phase-aligning them using a reference DEM, thereby effectively lowering the thermal noise floor and increasing the effective water/land contrast equivalently (see Appendix A). Nevertheless, comparing Figure 1 with Figure 2, we see that the land σ_0 in many cases is expected to be below or just slightly above the noise-equivalent σ_0 .

Let us now consider what is observed in a coherent power image, i.e. the power of the coherent sum of phase-aligned SLCs as described above and in Appendix A. Figure 3 shows an average cross-track profile of the coherent power of water and land computed on a simulated SWOT HR image. For water, the general cross-track trend is dominated by the antenna pattern. For land, it is almost flat because the land signal is dominated by instrument noise, mainly thermal noise in the receiver amplifiers, which is not shaped by the antenna pattern. It can easily be shown that the thermal noise in the complex raw image gives rise to a constant expected power (the thermal noise floor), but with fully developed speckle in the corresponding focused power image.

For conventional spaceborne SAR imaging applications, various radiometric calibration parameters are often compensated as part of the processing (e.g., see [18] for antenna pattern compensation for the case of TerraSAR-X). For SWOT viewing geometries the antenna pattern as well as the ground projected area factor vary significantly across the swath as a function of range or cross-track. The antenna pattern and the area factor can be accounted for either 1) by simply scaling the noisy measurement, or 2) by first subtracting a thermal noise estimate; however, both of these approaches can introduce artifacts. For example, simple scaling incorrectly applies the correction to the noise floor, while first subtracting a noisy estimate of the noise floor generally increases the dispersion of the distribution. For the example in Figure 3 simple scaling would flatten the water profile, but would make the land profile more variable as it is close to the thermal noise floor (it would give a profile similar to the inverse antenna pattern). For SWOT, the noise floor is relatively high compared to other sensors and so these radiometric compensations are not applied to the noisy data before water detection, but rather knowledge of the noise floor and the radiometric parameters are handled in the classification method itself.

On top of the general variations in power described above, there are also class-dependent incidence angle variations in the surface brightness (σ_0) as well as local variations in the surface properties. Local variations can be especially significant for water (spatial variations in wind speed and therefore water roughness, turbulence...), but to some extent also for land (related to topography, variations in soil roughness and humidity, vegetation...). Land variations are more likely to be observable in the middle of the swath where the SNR is more favorable.

III. PROPOSED WATER DETECTION APPROACH

Water detection in SWOT HR images is mainly based on the hypothesis that water is distinct from the land in terms of power brightness, as described above. The interferometric coherence is also generally higher for water than for land, but this is mainly because of the difference in SNR and therefore highly redundant with power. Although phase or height flatness could be used to inform water detection, this information is not considered at the stage of the processing where water detection occurs.

Our objective is therefore to use a SWOT HR coherent power image v to obtain a map of water areas u where:

$$u_i = \begin{cases} 1 & \text{if pixel } i \text{ should be classified as water and} \\ 0 & \text{if pixel } i \text{ should be classified as land.} \end{cases}$$

In the process of obtaining an estimate of this water map (binary water mask image in radar image coordinates), we also obtain estimates of the background land and water power images, which are parameters of the distribution of the measurement under the assumption of land and water, respectively. These background power images are needed for water detection, but are also updated/estimated from the measured data v and are useful estimates in other places in the SWOT algorithm chain (e.g., water fraction estimation to handle mixed-class-pixels when estimating water surface areas) [19].

A. Water Detection

In section I, we have mentioned several methods developed for water detection. In this paper, we consider Maximum A Posteriori classification: estimation of the water map u from the observation v is obtained by maximizing the posterior:

$$\hat{u} = \arg \max_u p(u|v) \quad (1)$$

From Bayes' theorem, this gives:

$$\hat{u} = \arg \max_u \frac{p(v|u)p(u)}{p(v)} \quad (2)$$

$$= \arg \max_u p(v|u)p(u) \quad (3)$$

$$= \arg \min_u -\log p(v|u) - \log p(u), \quad (4)$$

where two terms have to be modeled: a data-fidelity term $p(v|u)$ which relates the observations to the water map and a prior $p(u)$.

Water detection over inland areas can be seen as a binary classification problem with highly unbalanced classes: it is estimated that water covers about 2.5% [20] of the total continental surface of Earth. This can be expressed using a simple pixel-wise constant prior:

$$p(u_i = 0) = 0.975 \quad (5)$$

$$p(u_i = 1) = 0.025. \quad (6)$$

Note that a geographically varying prior probability of water can also be employed here (or even a convex combination of a constant and a geographically varying prior), but this is not considered in the scope of this paper. When used along with a separable data-fidelity term, this approach is a simple threshold. It is then strongly influenced by the presence of speckle. To reduce this effect, a regularization mechanism needs to be added.

Spatial regularization can be directly enforced using a Markov Random Field (MRF). Since the seminal work of Geman and Geman [21], MRFs have become a classical way of including spatial information in prior models. A suitable and widely-used prior for binary classification is the Ising model which penalizes neighbor pixels whose classes differ:

$$-\log p(u) = \beta \sum_{i \sim j} \psi(u_i, u_j) + k, \quad (7)$$

where the potential $\psi(u_i, u_j)$ is defined by

$$\psi(u_i, u_j) = \begin{cases} 0 & \text{if } u_i = u_j \text{ or,} \\ 1 & \text{if } u_i \neq u_j, \end{cases} \quad (8)$$

and where β is a weighting term and $i \sim j$ indicates that pixels i and j are neighbors in the considered neighborhood (in this article we use 4-connectivity). This prior, independently of the data term, favors spatially homogeneous outputs.

As we consider power observations, and under the hypothesis of fully developed speckle, we know from [22] that SAR power measurements follow a Gamma distribution. However, the use of the so-called coherent power is not conventional and its distribution is not well documented in the literature. Appendix A shows that the coherent power v also follows a Gamma distribution. A class is parametrized by its expected power μ and the effective number of looks L , allowing to model the observation using a Gamma likelihood. If we make the assumption that the likelihood is separable (which is a good assumption for SWOT because of the way the SAR images are focused and multilooked):

$$p(v|u) = \prod_i p(v_i|u_i) \quad (9)$$

$$= \prod_i \frac{1}{\Gamma(L)} \frac{L}{\mu_{u_i,i}} \left(\frac{Lv_i}{\mu_{u_i,i}} \right)^{L-1} \exp \left(\frac{-Lv_i}{\mu_{u_i,i}} \right), \quad (10)$$

where $\mu_{u_i,i}$ is the parameter of the Gamma distribution for the class u_i at pixel i representing the mean power. In the case of SWOT HR images, the multilooking operation conducted prior to water detection leads to $L \approx 4$. As explained in section II, the expected power μ of a class will vary throughout the image, and will here be considered to be an image itself, of the same size as the input radar image v .

To be explicit, there are two images for the parameters of the expected power μ , one under the assumption of water (μ_1), and another under the assumption of land (μ_0) for each pixel in the scene. These are sometimes referred to as the background land and water power images. A given pixel of the expected power image μ , denoted by $\mu_{u_i,i}$ for pixel i , can take on either the value of μ_0 or μ_1 for pixel i , depending on whether the class u_i corresponds to water or land.

Introducing (7) and (10) in (4) gives:

$$\hat{u} = \arg \min_u \mathcal{E}(u) \quad (11)$$

$$= \arg \min_u -\log(p(v|u)) - \log(p(u)) \quad (12)$$

$$= \arg \min_u \sum_i \left(L \log(\mu_{u_i,i}) + \frac{Lv_i}{\mu_{u_i,i}} \right) + \beta \sum_{i \sim j} \psi(u_i, u_j) \quad (13)$$

Note that it is also possible to include the prior coping with class imbalance introduced above in this model. Using an Ising model, the energy of (13) can be optimized by a graph-cut approach [23] computing the minimum cut in a flow graph. This reformulation allows to use the numerous methods developed in this area, giving a guarantee to find the global minimum. Compared to widely-used iterative methods such as simulated annealing [21], this method is very fast

and gives the exact optimum, which is very important from an operational point of view. For SWOT HR image tiles of approximately 3000×3000 pixels the computing time is on the order of 1 s for a consumer grade PC. The construction of the graph requires a lot of memory, on the order of 150 Bytes per pixel in our case, but for the SWOT HR image tile size mentioned above this is within the available memory per core on a modern computing cluster. To compute the min-cut, we use the algorithm proposed by [24], which is openly available and has been designed for regular graphs that are typically constructed for image processing applications. Further details are provided in the Appendix B.

B. Parameter estimation

The parameter images μ_0 and μ_1 (i.e., the background land and water power images) can be predicted based on the knowledge of the radar system, the topology and the expected σ_0 of both classes, or they can be estimated from the observed image and a (prior) water/land mask.

a) *From prior information*: The link between the expected value of the observed powers $E\{v\} = P_c$ and the σ_0 of the surfaces is provided by the so-called X-factor X , the so-called coherent gain G_c and the expected noise power N as follows

$$P_c = \sigma_0 X G_c + N. \quad (14)$$

Typical σ_0 values for water and land can be applied depending on whether we need the background water or land power. The X-factor is known from instrument calibration, the noise power is measured for each channel, the coherent gain can be estimated from the coherent power and two channel power measurements (see Appendix A).

b) *Markovian estimation*: While computing the parameters from prior information (14) allows to have non-constant parameters, it only takes into account variations coming from radar system (antenna pattern etc.) and prior knowledge of brightness and topography. However, as detailed in section II, there are also local variations in radar reflectivity or power, especially for water, because of variations in surface roughness. These variations can not realistically be predicted from prior data, but a certain spatial regularity can be expected, which we propose to model using a Gaussian MRF.

Let us assume that the map of water areas u is fixed, and that the parameter images μ_0 and μ_1 corresponding to the observed scene remain to be estimated.

We consider the logarithm of the power images (denoted \tilde{v} for the image v). When considering the logarithm of the image, the image is corrupted by an additive term ξ_i . This term follows a Fisher-Tippett distribution and can be considered to be approximately Gaussian when $L = 4$ [25]:

$$\tilde{v}_i = \tilde{\mu}_i + \tilde{\xi}_i \approx \tilde{\mu}_i + \eta_i, \quad (15)$$

where $\tilde{v} = \log v$, $\tilde{\mu} = \log \mu$ and η_i is Gaussian distributed with mean $m = \Psi(L) - \log L$ and variance $\Psi(1, L)$. Here $\Psi(\cdot)$ is the digamma function and $\Psi(\cdot, L)$ the polygamma function of order L .

We define one MRF for $\tilde{\mu}_0$ and one for $\tilde{\mu}_1$ (that we note $\tilde{\mu}_c, c \in \{0, 1\}$ in the following). We can estimate $\tilde{\mu}_c$ in a Bayesian framework, based on the knowledge of \tilde{v} and u :

$$-\log(p(\tilde{\mu}_c|\tilde{v}, u)) = -\log(p(\tilde{v}|\tilde{\mu}_c, u)) - \log(p(\tilde{\mu}_c)) \quad (16)$$

In the MRF of $\tilde{\mu}_c$, we define the data-term such that it takes into account the observation at pixels i where the water map is $u_i = c$. As we assumed the noise to be Gaussian distributed, the data term is simply the squared L2 distance between the model and the observation. In the cases where $u_i \neq c$, the data-term is set to a constant value (0 in our case):

$$-\log(p(\tilde{v}|\tilde{\mu}_c, u)) = \sum_i \begin{cases} (\tilde{v}_i - \tilde{\mu}_{c,i} - m)^2 & \text{if } u_i = c, \\ 0 & \text{otherwise.} \end{cases} \quad (17)$$

$$= \sum_i \bar{\delta}(u_i = c)(\tilde{v}_i - \tilde{\mu}_{c,i} - m)^2, \quad (18)$$

with:

$$\bar{\delta}(x) = \begin{cases} 1 & \text{if } x \text{ is true,} \\ 0 & \text{otherwise.} \end{cases} \quad (19)$$

The regularization term enforces spatial regularization. As more systematic variations in the range direction are expected (e.g., because of the antenna pattern), the spatial regularization is expressed as the sum of two terms: one for the range direction, the other for the azimuth. We add a third regularization term to avoid the result deviating too far from the prediction $\tilde{\mu}_{c,i}^0$ based on the thermal noise power, the X-factor, the coherent gain and the σ_0 hypotheses for class $c \in \{0, 1\}$ (14), giving:

$$\begin{aligned} -\log(p(\tilde{\mu}_c)) = & \beta_{az} \sum_{\substack{i \sim j \\ az}} (\tilde{\mu}_{c,i} - \tilde{\mu}_{c,j})^2 + \beta_{rg} \sum_{\substack{i \sim j \\ rg}} (\tilde{\mu}_{c,i} - \tilde{\mu}_{c,j})^2 \\ & + \beta_{th} \sum_i (\tilde{\mu}_{c,i} - \tilde{\mu}_{c,i}^0)^2. \end{aligned} \quad (20)$$

It gives the following MRFs to optimize:

$$\begin{aligned} \tilde{\mu}_0 &= \arg \min_{\mu} \mathcal{E}_0(\mu) \\ &= \arg \min_{\mu} \sum_i (1 - u_i)(\tilde{v}_i - \tilde{\mu}_i - m)^2 + \beta_{az} \sum_{\substack{i \sim j \\ az}} (\tilde{\mu}_i - \tilde{\mu}_j)^2 \\ &\quad + \beta_{rg} \sum_{\substack{i \sim j \\ rg}} (\tilde{\mu}_i - \tilde{\mu}_j)^2 + \beta_{th} \sum_i (\tilde{\mu}_i - \tilde{\mu}_{0,i}^0)^2 \end{aligned} \quad (21)$$

$$\begin{aligned} \tilde{\mu}_1 &= \arg \min_{\mu} \mathcal{E}_1(\mu) \\ &= \arg \min_{\mu} \sum_i u_i(\tilde{v}_i - \tilde{\mu}_i - m)^2 + \beta_{az} \sum_{\substack{i \sim j \\ az}} (\tilde{\mu}_i - \tilde{\mu}_j)^2 \\ &\quad + \beta_{rg} \sum_{\substack{i \sim j \\ rg}} (\tilde{\mu}_i - \tilde{\mu}_j)^2 + \beta_{th} \sum_i (\tilde{\mu}_i - \tilde{\mu}_{1,i}^0)^2 \end{aligned} \quad (22)$$

The energies \mathcal{E}_0 and \mathcal{E}_1 are quadratic in the unknown. Equations (21) and (22) are approximately solved by a few iterations of the conjugate gradients method (see subsection C). When initializing from a good initial guess (based on prior

data (14) or a parameter image from a previous acquisition of the same site), convergence of the conjugate gradients is fast.

Note that the third regularization term β_{th} introduces a bias toward the prior $\tilde{\mu}_{1,i}^0$ and must be used with caution (this bias is suppressed when β_{th} is equal to zero).

C. Iterative process

From (13), we see that the water detection step requires knowledge of the water and land class parameters. Conversely, estimation of the class parameters from the radar image requires a water map. To cope with this, we can use an iterative process to estimate both the water map u and the parameter images μ_0 and μ_1 . A similar method (for constant parameters) has been proposed in [26] with an initial classification obtained using a K-Means algorithm. In the case of the SWOT mission, we discussed in subsection III-Ba) that a first estimation of the parameters can be obtained theoretically. Therefore, the proposed iterative process starts with a first estimation of the parameters (μ_0^0, μ_1^0) based on prior information (14) to obtain a first classification u^0 . This classification is used to estimate better adapted parameters (μ_0^1, μ_1^1) , from which an improved classification u^1 is obtained. This process can be repeated until convergence or for a fixed number of times. A schematic representation of the algorithm is given in Figure 4. Note that the convergence of this iterative process is not guaranteed, and will have to be reassessed when real data become available. We will then typically start without iteration, and gradually increase the number of iterations, depending on the observed convergence.

IV. RESULTS

As the satellite has not yet been launched, the performance of the proposed method has been assessed on simulated data sets. The work in this section shows the feasibility of the method for SWOT application as well as a general characterization of its performance on a limited data set. A complete validation of the method in the context of SWOT ground processing is beyond the scope of this paper and is an ongoing effort among the SWOT ADT.

A. Experiments

a) Dataset: the proposed method has been tested on simulated SWOT HR image extracts over two areas:

- the Po river in Italy (based on input data from [27])
- the Camargue area in France

The prior information needed to predict the expected water and land powers (14) were available for the first image, simulated with JPL's HR science simulator (build 1051), but not for the second image, obtained with the CNES HR simulator [28]. The main characteristics of the images are presented in Table I.

b) Methods: for each image, we compute the results with the following methods:

- **MAP:** thresholding method according to the maximum a posteriori estimation using the pixel-wise constant priors

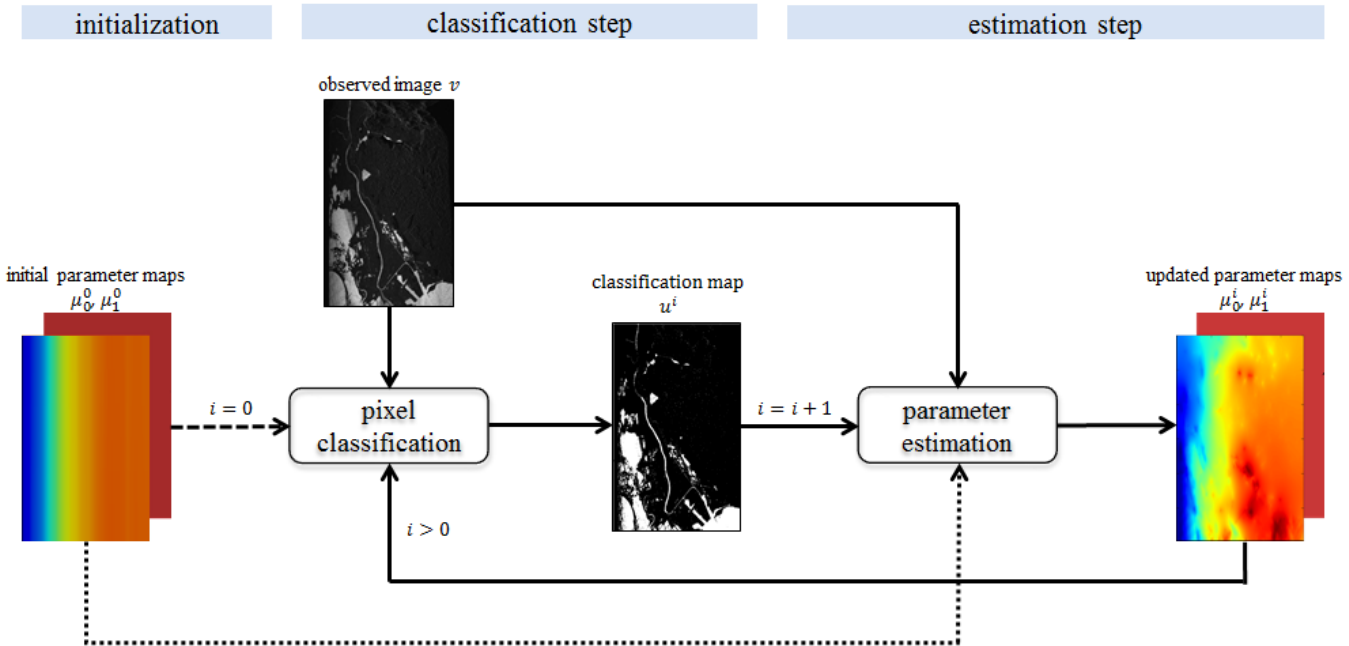


Fig. 4. A first classification \mathbf{u}^0 is obtained from initial parameters μ_0^0 and μ_1^0 . This classification is then used to estimate new class parameters μ_0^1 and μ_1^1 , which are used to obtain a new classification \mathbf{u}^1 . The process is then repeated for a given number of times.

TABLE I
CHARACTERISTICS OF THE DATA USED FOR THE EVALUATION OF THE METHODS

	Po	Camargue
Origin	JPL SWOT HR science simulator	CNES SWOT HR simulator
Band	Ka (35.75GHz)	
Incidence angle	0.6 - 3.9°	
Resolution (azimuth × range)	70m-10m × 5m	
Size (azimuth × range)	1517 × 3108	2979 × 1839
Ground truth	from simulator	

given by (5) and (6). The parameters μ_0 and μ_1 are predicted from prior information (14).

- **MRF**: Markovian water detection (13) with the same μ_0 and μ_1 obtained from prior information (14).
 - **MRF with Markovian parameter estimation** (proposed model): Markovian water detection (13) with parameters estimated from (21) and (22), using the iterative scheme introduced in subsection III-C.

Note that for the second image, as the needed prior information are not available, we have replaced the (initial) parameter maps μ_0 and μ_1 by constant scalar values computed using the ground truth.

c) *Metrics*: in this study, we report the following metrics:

$$\text{TPR} \text{ (or Recall)} = \frac{TP}{TP + FN}, \quad (23)$$

$$\text{FPR} = \frac{FP}{FP + TN}, \quad (24)$$

$$\text{Precision} = \frac{TP}{TP + FP}, \quad (25)$$

$$\text{F-score} = 2 \frac{\text{Precision} \times \text{Recall}}{\text{Precision} + \text{Recall}}, \quad (26)$$

$$\text{ER} = \frac{FP + FN}{TP + FN}, \quad (27)$$

$$\text{MCC} = \frac{TP \times TN - FP \times FN}{\sqrt{(TP + FN)(FP + TN)(TP + FP)(TN + FN)}}, \quad (28)$$

where TP, TN, FP, FN are the number of true positives, true negatives, false positives and false negatives with respect to the water class. TPR is the true positive rate (or recall), FPR is the false positive rate, and F-score is the harmonic mean of precision and recall. The relative Error Rate (ER) is close to the metric of the science requirements of the SWOT mission [3], except that the latter computes ground-projected surfaces ($\text{in } m^2$) and only considers detected water pixels near water bodies identified in a separate river and lake database. Without this distance constraint, the ER presented here is impacted by the fact that there is generally much more land than water in a scene: the more land, the more frequent are the false positives. We also report the Matthew's Correlation Coefficient (MCC) to take into account this over-representation of land. MCC gives a score between -1 and 1, where 0 would be a random prediction and 1 a perfect result.

B. Results and discussion

The quantitative results are reported in Table II and visual representations are proposed in Figure 5 for the image of the Po river, and in Figure 6 for the image of the Camargue area.

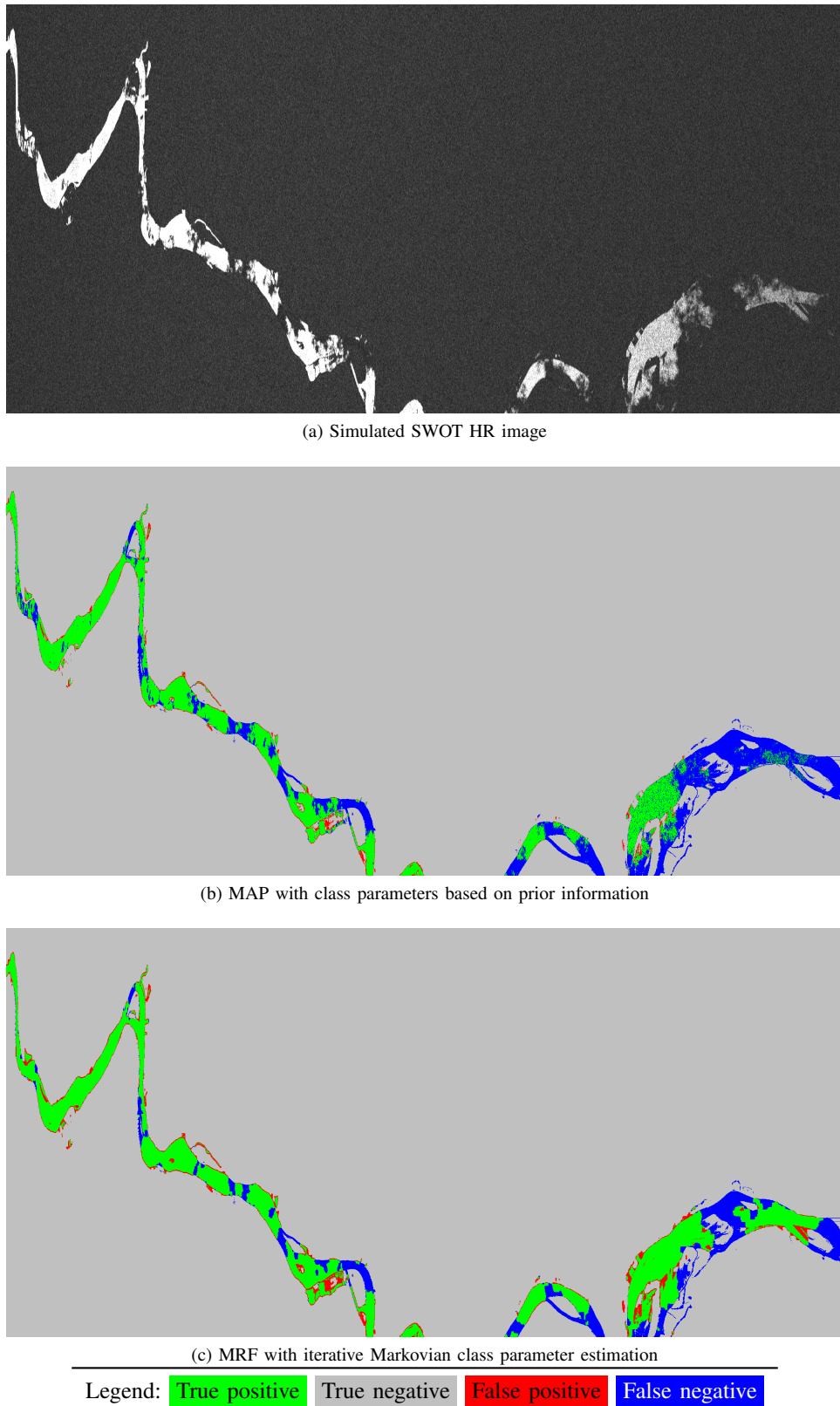


Fig. 5. Water detection results obtained on a simulated SWOT HR image of the Po river. The water surfaces appear as bright areas in the image (a), except in regions with low wind. Classification based on prior information of the class parameters (b) is less accurate than with the proposed MRF model (c).

TABLE II

RESULTS ON THE CONSIDERED DATASET. FOR EACH IMAGE, WE EVALUATED THE PROPOSED METHOD (MRF ESTIMATED PARAMETERS) AGAINST TWO CLASSICAL APPROACHES.

Image	Method	TPR	FPR	Precision	F-score	ER	MCC
Po	MAP	53.36%	0.33%	91.09%	67.30%	51.86%	0.6839
	MRF constant	72.93%	0.79%	85.47%	78.70%	39.47%	0.7774
	MRF estimated parameters	74.24%	0.80%	85.46%	79.45%	38.40%	0.7847
Camargue	MAP	39.94%	0.32%	96.07%	56.43%	61.69%	0.5817
	MRF constant	93.16%	2.95%	86.21%	89.55%	21.74%	0.8748
	MRF estimated parameters	91.80%	2.18%	89.28%	90.52%	19.22%	0.8863

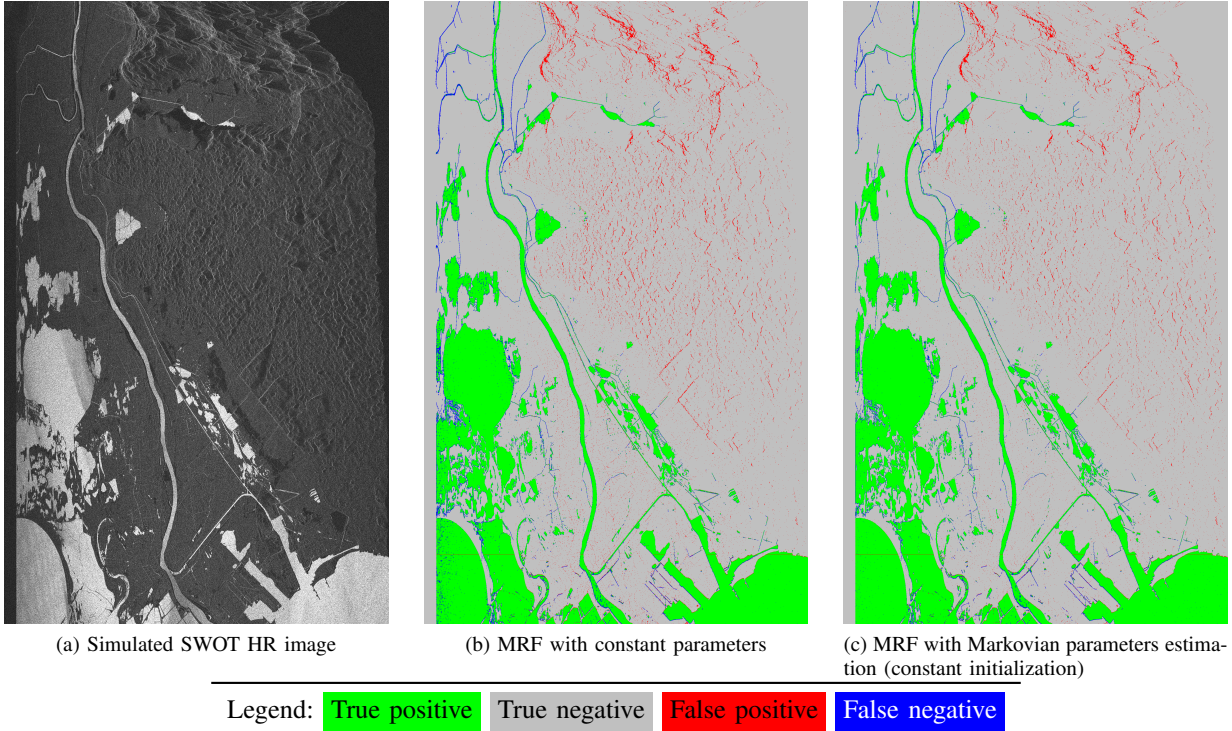


Fig. 6. Water detection results obtained on a simulated SWOT HR image of the Camargue area. The layover phenomenon, visible in the upper right part of the image (a), causes false detection of water. Estimating spatially variable parameters improves the classification (c) compared to the use of constant parameters (b).

As can be seen in Figure 5a), the image of Po exhibits patches of "dark water" as described in section II. In such cases the Markovian methods (especially with the Markovian re-estimation of class parameters) give much better results. Nevertheless, it should be noted that correctly detecting dark water is not explicitly needed in this stage of the SWOT processing and is handled later in the processing chain. The Camargue image contains numerous layover areas and a much lower contrast than the two previous images. Due to the poor contrast, the pixel-wise MAP performs poorly as it is strongly affected by the speckle. Furthermore, the Markovian re-estimation of class parameters allows to strongly reduce the quantity of land/land layover detected as water.

Except in favorable cases where the contrast between water and land is particularly high, the methods with MRF regularization give better results than the pixel-wise MAP. Note that it would be possible to increase the TPR of the MAP method by lowering $p(u_i = 0)$ in Equation (5) (and increasing $p(u_i = 1)$ in Equation (6)), at the cost of much higher FPR. Furthermore, the proposed re-estimation of class

parameters using a Gaussian Markov Random Field generally gives better results as it improves the robustness to local variations (for example due to layover or "dark water"). It should be noted that the experiments presented in this study are based on simulated images, and that the initial class parameters predicted from prior information (14) are likely to be more accurate than what will be available for real images. The proposed Markovian estimation scheme should improve the robustness to these discrepancies. Therefore, while the spatial parameters β_{az} and β_{rg} can be set to a fixed value (in our study, we empirically set $\beta_{az} = 130$ and $\beta_{rg} = 500$), β_{th} needs to be tuned with respect to the estimated quality of the initial class parameters.

In summary, the method proposed in this paper for detecting and spatially regularizing water areas in SWOT images generally out performs the more classical pixel-wise MAP approach. Therefore, this method is being considered in the baseline ground processing, and is currently being investigated further in the context of more general SWOT performance assessments among the SWOT ADT.

V. CONCLUSION

In this article, we have presented a method for water detection in the HR images of the future SWOT mission. The originality of the method is to use a Gaussian MRF to regularize the estimation of spatially variable class parameters, as part of an iterative process where another MRF is used in the actual water detection. We have shown on simulated images that the proposed method allows to be more robust to local variations in the backscattering. Because of the added robustness, the method in this paper has been identified as a candidate for baseline ground processing of the SWOT data and will continue to be investigated and assessed among the SWOT ADT. Future developments will include water-fraction estimation, dark-water flagging, as well as handling of bright land. Narrow rivers are particularly challenging to detect and may require specific methods, such as the one proposed in [29]. Multitemporal and multi-sensor water detection are other interesting options that may be addressed in future investigations.

ACKNOWLEDGMENT

The authors would like to thank CNES and the Futur&Ruptures program of the Fondation Mines-Télécom for the funding of the PhD of S. Lobry. We acknowledge Victor Poughon, Manuel Grizonnet and Damien Desroches (CNES), as well as Lucie Labat-Allé (C-S), for support on simulations and processing. We also thank Alessio Domeneghetti (Università di Bologna, Italy) for providing the input data to the simulation of the Po river image.

A portion of this work was carried out at the Jet Propulsion Laboratory, California Institute of Technology, under a contract with the National Aeronautics and Space Administration.

APPENDIX

A. Coherent Power

The so-called coherent power can be thought of as the power of a coherent average of the two SLC images, where the phase of the slave image has been rotated by a reference phase. As will be shown, this approach enables an SNR gain of up to a factor of 2, which for relatively low SNR systems like SWOT can significantly improve performance. The coherent power can thus be computed directly from the SLC images (z_1 and z_2) and the flattening reference phase (ϕ_{ref}). The coherent average of the SLCs can be expressed as

$$z_c = \frac{z_1 + z_2 e^{-j\phi_{ref}}}{2}. \quad (29)$$

The noisy measurement of the single-look coherent power is

$$p_c = 2|z_c|^2 = 2z_c z_c^*, \quad (30)$$

where the factor of 2 makes the coherent power scaled consistent with the single channel powers (i.e., scaled similar to averaging the powers as opposed to averaging the SLCs). Furthermore, if we multilook this power over n_i pixels we obtain the measurement used for water detection

$$\mathbf{v} = \frac{1}{n_i} \sum_i p_c. \quad (31)$$

It can be shown that the multilooked coherent power can also be expressed as

$$\mathbf{v} = \frac{p_1 + p_2}{2} + \Re\{I\} \quad (32)$$

$$= \frac{p_1 + p_2}{2} + |I| \cdot \cos(\angle I). \quad (33)$$

where $I = \frac{1}{n_i} \sum_i z_1 z_2^* e^{j\phi_{ref}}$ is the multilooked flattened interferogram, and $p_1 = \frac{1}{n_i} \sum_i |z_1|^2$ and $p_2 = \frac{1}{n_i} \sum_i |z_2|^2$ are the multilooked two channel powers. This form facilitates the use of coherent power after interferogram formation and multilooking are performed, without needing to have access to the original SLCs.

a) Coherent Power Distribution: In order to develop a water detection algorithm, it is important to know the distribution of the measurement. We will now show that multilooked coherent power is Gamma distributed, just like the single-channel powers. First, observe that z_1 and z_2 are correlated zero-mean complex Gaussian random variables with covariance [30]

$$\Gamma = \begin{bmatrix} P_1 & \gamma\sqrt{P_1 P_2} e^{-j\phi} \\ \gamma\sqrt{P_1 P_2} e^{j\phi} & P_2 \end{bmatrix} \quad (34)$$

$$= \begin{bmatrix} \sigma_0 X_1 + N_1 & \gamma_s \sigma_0 \sqrt{X_1 X_2} e^{-j\phi} \\ \gamma_s \sigma_0 \sqrt{X_1 X_2} e^{j\phi} & \sigma_0 X_2 + N_2 \end{bmatrix}, \quad (35)$$

where $P_1 = \sigma_0 X_1 + N_1$ and $P_2 = \sigma_0 X_2 + N_2$ are the two channel signal-plus-noise powers, N_1 and N_2 are the expected noise powers, X_1 and X_2 are the X-factor radiometric calibration parameters, σ_0 is the scene backscatter brightness (normalized radar cross-section), ϕ is the interferometric phase, γ_s is the signal-only interferometric coherence, and γ is the coherence with the thermal component, i.e., $\gamma = \gamma_s \gamma_{SNR}$, where [31]

$$\gamma_{SNR} = \frac{1}{\sqrt{(1+SNR_1^{-1})(1+SNR_2^{-1})}}, \quad (36)$$

and $SNR_k = \frac{X_k \sigma_0}{N_k}$ for $k \in [0, 1]$.

The two-channel SLC measurements can be expressed as a combination of independent, uncorrelated circular Gaussians as follows

$$z_1 = \sqrt{P_1} (\sqrt{\gamma} \nu_0 + \sqrt{1-\gamma} \nu_1) \quad (37)$$

$$z_2 = \sqrt{P_2} (\sqrt{\gamma} \nu_0 + \sqrt{1-\gamma} \nu_2) e^{j\phi}, \quad (38)$$

where ν_0 , ν_1 , and ν_2 are independent zero-mean circular Gaussian random variables with unit covariance. Note that this is a typical approach to simulate correlated complex Gaussian random variables (e.g., InSAR measurements). The coherent average of the SLC images (z_c) can now be expressed as

$$z_c = \frac{1}{2} \left(\nu_0 \sqrt{\gamma} (\sqrt{P_1} + \sqrt{P_2} e^{j\Delta\phi}) + \nu_1 \sqrt{P_1(1-\gamma)} + \nu_2 \sqrt{P_2(1-\gamma)} e^{j\Delta\phi} \right), \quad (39)$$

where $\Delta\phi = \phi - \phi_{ref}$ is the flattened phase.

Note that z_c is a zero-mean complex Gaussian, since it is a weighted sum of independent zero-mean complex Gaussians.

The distribution of z_c is fully determined by the covariance, which can be expressed as

$$E|z_c|^2 = \frac{P_1 + P_2}{4} + \frac{\gamma\sqrt{P_1 P_2} \cos(\Delta\phi)}{2} \quad (40)$$

$$= \frac{\sigma_0(X_1 + X_2) + N_1 + N_2}{4} \quad (41)$$

$$+ \frac{\gamma_s \sigma_0 \sqrt{X_1 X_2} \cos(\Delta\phi)}{2},$$

Since z_c is zero-mean complex Gaussian and represents a single look, $|z_c|^2$, and p_c are exponentially distributed. Multilooking p_c then produces a Gamma distributed random variable v , similar to the single channel multilooked power measurements [22]. Nevertheless, the SNR of the coherent power is generally improved (at most by a factor of 2) compared to the single-channel powers (as well as the average of the two powers) as we will now show.

b) *Coherent Gain*: Now let us assume $N_1 = N_2 = N$ and $X_1 = X_2 = X$, which is approximately true if the two channels have similar antenna patterns, are well calibrated, and have similar noise characteristics (which is the case for SWOT). Also, let us assume that we multilook independent pixels, whose distributions are the same (i.e., X , N , σ_0 , and γ_s are the same for all pixels), except for possibly the flattened phase (i.e., we do not require $\Delta\phi$ to be the same for all pixels, represented as $\Delta\phi_i$). Then the expected coherent power P_c can be expressed as

$$P_c = E\{v\} = \frac{1}{n_i} \sum_i E\{p_c\} = \frac{2}{n_i} \sum_i E\{|z_c|^2\} \quad (42)$$

$$= \frac{1}{n_i} \sum_i (X\sigma_0(1 + \gamma_s \cos(\Delta\phi_i)) + N) \quad (43)$$

$$= N + \sigma_0 X \frac{1}{n_i} \sum_i (1 + \gamma_s \cos(\Delta\phi_i)). \quad (44)$$

Under the assumptions stated above, the SNR for each of the single channels can be expressed as $\text{SNR}_0 = \frac{X\sigma_0}{N}$. The SNR of the coherent power case is the ratio of the thermal-noise-free expected coherent power $P_c - N$ and the expected noise power N , which can be expressed as

$$\text{SNR}_c = \frac{P_c - N}{N} \quad (45)$$

$$= \frac{\sigma_0 X \frac{1}{n_i} \sum_i (1 + \gamma_s \cos(\Delta\phi_i))}{N} \quad (46)$$

$$= \text{SNR}_0 \frac{1}{n_i} \sum_i (1 + \gamma_s \cos(\Delta\phi_i)). \quad (47)$$

Thus, the SNR of the coherent power is a scaled version of the single channel SNR by a factor called the coherent gain

$$G_c = \frac{1}{n_i} \sum_i (1 + \gamma_s \cos(\Delta\phi_i)). \quad (48)$$

The coherent gain varies between 0 and 2, and peaks when the reference phase is a good estimate of the true phase. An estimate of the coherent gain can be computed from the ratio of the two channel powers and the coherent power.

Note that if we have a poor estimate of phase, this coherent gain approach may actually degrade the signal. For example,

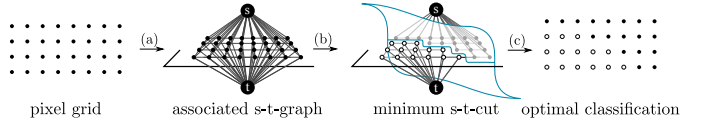


Fig. 7. Classification of image pixels by graph-cuts is performed in 3 steps: (a) construction of a s-t-graph where each pixel of the original image is given a node in the corresponding graph; (b) computation of the minimum cost s-t-cut; (c) identification of the optimal binary label for each pixel based on the connection severed by the optimal cut.

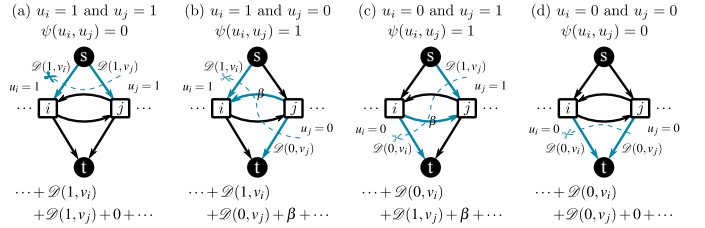


Fig. 8. The graph shown in figure 7 is built in such a way that s-t-cuts are in bijection with binary labelings of the image. Cases (a) to (d) represent the 4 configurations of neighboring nodes i and j . The cost of the cut exactly matches the value of the energy defined in our Markovian modeling.

as long as the error between the true phase and the reference phase large $|\Delta\phi_i| > 90^\circ$, the term inside the sum is less than 1, which can produce power attenuation rather than gain if it is consistently low over the area being multilooked. Therefore, it is important to have a reference DEM that produces small $\Delta\phi_i$. The SWOT processor has a filter to check for this case to ensure there is always signal amplification of the SNR, rather than attenuation.

B. Pixel classification by graph-cuts

Under our Markov random field model, estimation of the classification \hat{u} is performed by solving the minimization problem given in (13). This minimization takes the form:

$$\arg \min_{\mathbf{u}} \sum_i \mathcal{D}(u_i, v_i) + \beta \sum_{i,j} \psi(u_i, u_j), \quad (49)$$

where $\mathcal{D}(u_i, v_i) = L \log(\mu_{u_i, i}) + L \frac{v_i}{\mu_{u_i, i}}$ is a data term that enforces the classification to select labels such that the expected power $\mu_{u_i, i}$ of the class u_i at pixel i is likely given the observed intensity v_i . Since the first sum involves only terms depending on the label at a given pixel and the second sum penalizes by a factor β neighboring pixels with different labels, the energy minimization problem can be solved by graph-cuts.

Figure 7 outlines the approach followed to solve the minimization by graph-cuts. In a first step, Fig.7(a), an s-t-graph is built. Two nodes play a particular role in this flow network: the source s and the sink t . In addition to these two special nodes, nodes are created to represent each pixel of the image to classify. These nodes are all connected to the source and to the sink. To enforce the spatial regularization, pairs of edges are also created between nodes that represent neighboring pixels $i \sim j$ in the original image. A capacity (non-negative value) is affected to each edge of the graph so that a flow can be defined over the graph. By Ford-Fulkerson's max flow / min-cut theorem, the maximum flow that can be defined over the

s-t-cut while respecting (i) the capacity of each edge (the flux flowing over a given edge is a non-negative value that is less or equal to the edge capacity) and (ii) the non-accumulation condition (the sum of fluxes entering a node equals the sum of fluxes leaving the node, for all nodes except the source and sink) indicates the minimum cut of the graph, Fig.7(b). This minimum cut can be mapped into the optimal classification \hat{u} , Fig.7(c).

In order to separate the graph into two partitions, one containing the source, the other containing the sink, a cut necessarily severs either the edge connecting node i to the source, or the edge connecting i to the sink. By convention, when the source edge is severed, node i is given label 1, otherwise, node i is given label 0. Figure 8 illustrates how the capacities of the edges are set in order to guarantee that the cost of all possible s-t-cuts be in bijection with the energy of the corresponding binary field u . Edges from the source to node i and from i to the sink are given capacities $\mathcal{D}(1, v_i)$ and $\mathcal{D}(0, v_i)$, respectively. Pairs of edges connecting neighboring nodes i and j are given the capacity β . That way, in each of the 4 configurations represented in Fig.8(a)-(d) for two neighboring pixels i and j , the cost of the cut (*i.e.*, the sum of the capacities of all edges severed by the cut that are oriented downstream) exactly matches the value of the terms in the energy minimization problem of (49).

To build the graph, compute the maximum flow and identify the minimum cut, we used the open-source library described in [24].

C. Conjugate gradient optimization of GMRF estimation

To optimize the MRFs of (21) and (22), we use the conjugate gradients method. In this subsection, we detail the computation for (22), the optimization of (21) being similar. The gradient of \mathcal{E}_1 is:

$$\begin{aligned} \frac{d\mathcal{E}_1}{d\mu_1} = & 2 \left(u_i (\tilde{\mu}_{1,i} - \tilde{v}_i) + \beta_{az} \sum_{i \sim j} (\tilde{\mu}_{1,i} - \tilde{\mu}_{1,n}) \right. \\ & \left. + \beta_{rg} \sum_{i \sim j} (\tilde{\mu}_{1,i} - \tilde{\mu}_{1,n}) + \beta_{th} (u_i (\tilde{\mu}_{1,i} - \tilde{\mu}_{0,i})) \right) \quad (50) \end{aligned}$$

To use the conjugate gradients method, we need to formulate our problem as:

$$A\tilde{\mu}_{1v} = b, \quad (51)$$

where $\tilde{\mu}_{1v}$ is the vectorized version of $\tilde{\mu}_1$. It gives:

$$A\tilde{\mu}_{1v} = (2 + 2\beta_{th})\text{diag}(\mathbf{u})\tilde{\mu}_{1v} + 2D^t D\tilde{\mu}_{1v}, \quad (52)$$

where $D^t D$ is a band matrix encoding the neighborhood (an example is given in Figure 9), and

$$b = 2\text{diag}(\mathbf{u})\tilde{v} + 2\beta_{th}\text{diag}(\mathbf{u})\tilde{\mu}_1^0 \quad (53)$$

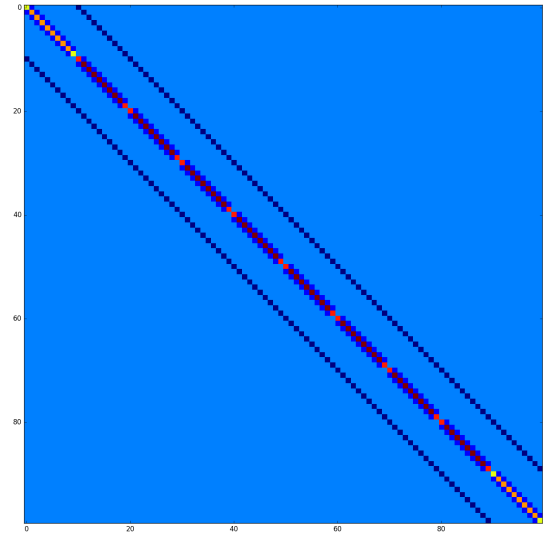


Fig. 9. Sample $D^t D$ matrix for a 10×10 image. This matrix encodes the relations between neighbors according to the values of β_{az} and β_{th} .

REFERENCES

- [1] L.-L. Fu, D. Alsdorf, R. Morrow, E. Rodriguez, and N. Mognard, “SWOT: the Surface Water and Ocean Topography Mission: wide-swath altimetric elevation on Earth,” Jet Propulsion Laboratory, National Aeronautics and Space Administration, JPL Publication 12-05, 2012.
- [2] M. Durand, L. Fu, D. P. Lettenmaier, D. E. Alsdorf, E. Rodriguez, and D. Esteban-Fernandez, “The surface water and ocean topography mission: Observing terrestrial surface water and oceanic submesoscale eddies,” *Proceedings of the IEEE*, vol. 98, no. 5, pp. 766–779, May 2010.
- [3] E. Rodríguez, “Surface Water and Ocean Topography Mission (SWOT): Science Requirements Document,” *SWOT NASA/JPL Project, Pasadena, California*. Available at https://swot.jpl.nasa.gov/files/swot/SRD_021215.pdf, 2014.
- [4] H. Liu and K. C. Jezek, “Automated extraction of coastline from satellite imagery by integrating canny edge detection and locally adaptive thresholding methods,” *International Journal of Remote Sensing*, vol. 25, no. 5, pp. 937–958, 2004.
- [5] J.-S. Lee, “Speckle analysis and smoothing of synthetic aperture radar images,” *Computer Graphics and Image Processing*, vol. 17, no. 1, pp. 24 – 32, 1981.
- [6] P. Perona and J. Malik, “Scale-space and edge detection using anisotropic diffusion,” *IEEE Transactions on pattern analysis and machine intelligence*, vol. 12, no. 7, pp. 629–639, 1990.
- [7] C. Cazals, S. Rapinel, P.-L. Frison, A. Bonis, G. Mercier, C. Mallet, S. Corgne, and J.-P. Rudant, “Mapping and characterization of hydrological dynamics in a coastal marsh using high temporal resolution Sentinel-1A images,” *Remote Sensing*, vol. 8, no. 7, p. 570, 2016.
- [8] Z. Xu, Q. Shi, Y. Chen, W. Feng, Y. Shao, L. Sun, and X. Huang, “Non-stationary speckle reduction in high resolution SAR images,” *Digital Signal Processing*, vol. 73, pp. 72–82, 2018.
- [9] J. Chen, Q. Wang, J. Wang, and N. Li, “Change detection of water index in Danjiangkou reservoir using mixed log-normal distribution based active contour model,” *IEEE Access*, vol. 7, pp. 95 430–95 442, 2019.
- [10] C.-A. Deledalle, L. Denis, F. Tupin, A. Reiniger, and M. Jager, “NL-SAR: A Unified Nonlocal Framework for Resolution-Preserving (Pol)(In)SAR Denoising,” *Geoscience and Remote Sensing, IEEE Transactions on*, vol. 53, no. 4, pp. 2021–2038, April 2015.
- [11] R. Touzi, A. Lopes, and P. Bousquet, “A statistical and geometrical edge detector for SAR images,” *IEEE Transactions on Geoscience and Remote Sensing*, vol. 26, no. 6, pp. 764–773, 1988.
- [12] R. Fjørtoft, A. Lopes, P. Marthon, and E. Cubero-Castan, “An optimal multiedge detector for SAR image segmentation,” *IEEE Transactions on Geoscience and Remote Sensing*, vol. 36, no. 3, pp. 793–802, 1998.
- [13] L. Najman and M. Schmitt, “Geodesic saliency of watershed contours and hierarchical segmentation,” *IEEE Transactions on Pattern Analysis and Machine Intelligence*, vol. 18, pp. 1163–1173, December 1996.

- [14] M. Silveira *et al.*, "Separation Between Water and Land in SAR Images Using Region-Based Level Sets," *IEEE Geoscience and Remote Sensing Letters*, vol. 6, no. 3, pp. 471–475, July 2009.
- [15] T. F. Chan and L. A. Vese, "Active contours without edges," *IEEE Transactions on Image Processing*, vol. 10, no. 2, pp. 266–277, 2001.
- [16] R. Fjørtoft, J.-M. Gaudin, N. Pourthie, J.-C. Lalaurie, A. Mallet, J.-F. Nouvel, J. Martinot-Lagarde, H. Oriot, P. Borderies, C. Ruiz, and S. Daniel, "KaRIn on SWOT: Characteristics of Near-Nadir Ka-Band Interferometric SAR Imagery," *IEEE Transactions on Geoscience and Remote Sensing*, vol. 52, no. 4, pp. 2172–2185, April 2014.
- [17] D. E. Fernandez, "SWOT Project Mission Performance and Error Budget," Jet Propulsion Laboratory, JPL D-79084, 2017.
- [18] M. Bachmann, M. Schwerdt, and B. Brautigam, "TerraSAR-X antenna calibration and monitoring based on a precise antenna model," *IEEE Transactions on Geoscience and Remote Sensing*, vol. 48, no. 2, pp. 690–701, 2010.
- [19] B. Williams and D. Desroches, "Level 2 KaRIn high rate pixel cloud algorithm theoretical basis document," Jet Propulsion Laboratory, Tech. Rep., in preparation.
- [20] P. H. Gleick, *Water in crisis: a guide to the world's fresh water resources*. Oxford University Press, New York, 1993.
- [21] S. Geman and D. Geman, "Stochastic Relaxation, Gibbs Distributions, and the Bayesian Restoration of Images," *IEEE Transactions on Pattern Analysis and Machine Intelligence*, vol. PAMI-6, no. 6, pp. 721–741, Nov 1984.
- [22] J. W. Goodman, *Speckle phenomena in optics: theory and applications*. Roberts and Company Publishers, 2007.
- [23] D. Greig, B. Porteous, and A. H. Seheult, "Exact maximum a posteriori estimation for binary images," *Journal of the Royal Statistical Society. Series B (Methodological)*, pp. 271–279, 1989.
- [24] Y. Boykov and V. Kolmogorov, "An experimental comparison of min-cut/max-flow algorithms for energy minimization in vision," *IEEE Transactions on Pattern Analysis and Machine Intelligence*, vol. 26, no. 9, pp. 1124–1137, 2004.
- [25] Hua Xie, L. E. Pierce, and F. T. Ulaby, "Statistical properties of logarithmically transformed speckle," *IEEE Transactions on Geoscience and Remote Sensing*, vol. 40, no. 3, pp. 721–727, March 2002.
- [26] R. Fjørtoft, Y. Delignon, W. Pieczynski, M. Sigelle, and F. Tupin, "Unsupervised classification of radar images using hidden Markov chains and hidden Markov random fields," *IEEE Transactions on Geoscience and Remote Sensing*, vol. 41, no. 3, pp. 675–686, 2003.
- [27] A. Domeneghetti, G. Schumann, R. P. M. Frasson, R. Wei, T. Pavelsky, A. Castellarin, A. Brath, and M. Durand, "Characterizing water surface elevation under different flow conditions for the upcoming SWOT mission," *Journal of Hydrology*, vol. 561, April 2018.
- [28] F. Soulard, J. Duro, R. Fjørtoft, P. Dubois, X. Banque, R. Robledo, D. Desroches, J.-M. Gaudin, N. Pourthie, D. Carbonne, and N. Picot, "Simulation of near-nadir bistatic InSAR data in Ka-band for the SWOT mission," in *IEEE International Geoscience and Remote Sensing Symposium (IGARSS)*, July 2015.
- [29] S. Lobry, F. Tupin, and R. Fjørtoft, "Unsupervised detection of thin water surfaces in SWOT images based on segment detection and connection," in *IEEE International Geoscience and Remote Sensing Symposium (IGARSS)*, July 2017, pp. 3720–3723.
- [30] R. J. A. Tough, D. Blacknell, and S. Quegan, "A statistical description of polarimetric and interferometric synthetic aperture radar data," *Proceedings of the Royal Society*, 1995.
- [31] P. A. Rosen, S. Hensley, I. R. Joughin, F. K. Li, S. N. Madsen, E. Rodriguez, and R. M. Goldstein, "Synthetic aperture radar interferometry," *Proceedings of the IEEE*, vol. 88, no. 3, 2000.



Sylvain Lobry (S16 - M17) received the Engineering degree from Ecole pour l'Informatique et les Techniques Avancées (EPITA), Kremlin Bicêtre, France in 2013, the Masters degree in science and technology from the University Pierre et Marie Curie (Paris 6), Paris in 2014, and the Ph.D. degree from Telecom Paris, Paris, France, in 2017. He is currently a Post-Doctoral Researcher with the Geo-Information Science and Remote Sensing Laboratory, Wageningen University, The Netherlands. His research interests include radar image processing and multimodal processing of heterogeneous satellite data.



Loïc Denis received the M.Sc. degree from CPE Lyon, Villeurbanne, France, in 2003, and the Ph.D. degree from the Université de Saint-Etienne, Saint-Etienne, France, in 2006. He is currently an Associate Professor with the Université de Lyon, Lyon, France. His research interests include image denoising and reconstruction, radar image processing, deconvolution, holographic microscopy and exoplanet detection. Dr. Denis was a co-recipient of the IEEE ICIP Best Student Paper Award in 2010, the EURASIP EUSIPCO Best Student Paper Award in 2010, and the IEEE Geoscience and Remote Sensing Society 2016 Transactions Prize Paper Award.



Brent Williams obtained his PhD in electrical and computer engineering from Brigham Young University in 2010 and is currently a member of the Radar Algorithms and Processing group at the NASA Jet Propulsion Laboratory, California Institute of Technology. Dr. Williams is the algorithm-development lead for the SWOT science processor that performs water detection, phase unwrapping, layover flagging, and geolocation of the high-resolution interferometric data.



Roger Fjørtoft (M'01) received the M.S. degree in electronics from the Norwegian Institute of Technology, Trondheim, Norway, in 1993, and the Ph.D. degree in signal processing, image processing, and communications from the Institut National Polytechnique, Toulouse, France, in 1999. He was a Senior Research Scientist with the Norwegian Computing Center, Oslo, Norway, from 2000 to 2003, and has since then been with the French Space Agency, Centre National d'Etudes Spatiales (CNES), Toulouse, France. Dr. Fjørtoft is currently with the Radar Algorithms, Processing and Products Department (DSO/SI/TR), where he leads the development of algorithms for the operational processing of high-resolution data from the upcoming SWOT mission, prepared jointly by NASA/JPL and CNES.



Florence Tupin (SM07) received the Engineering degree and the Ph.D. degree in signal and image processing from Ecole Nationale Supérieure des Télécommunications (ENST), Paris, France, in 1994 and 1997, respectively, and the Habilitation Diriger des Recherches degree from the University of Rennes, Rennes, France, in 2007. From 1997 to 1998, she was with SAGEM, Paris, where she focused on fingerprint recognition. Since 1998, she has been an Associate Professor and then a Professor of image and signal processing with the Image, Data, Signal Department, ENST, where she is currently a Professor. Since 2014, she has been the Head of the Image, Modeling, Analysis, GEometry, and Synthesis Group, LTCI, Telecom Paris, Paris, France. She has co-authored over 200 papers. Her research interests include image processing and analysis, especially for remote sensing and synthetic aperture radar imagery applications, and earth observation. Dr. Tupin has been a member of the international and national technical committees since 2003. She was the Chair of the Urban Remote Sensing Joint Event held in Paris in 2007. She was an Associate Editor of the French Journal Signal Processing from 2005 to 2007 and the IEEE Transactions on Geoscience and Remote Sensing from 2007 to 2016. She received several awards, among them the IEEE TGRS Transactions Prize Paper Award in 2016 for works on nonlocal speckle filtering.